RSC Advances

PAPER

View Article Online
View Journal | View Issue

Cite this: *RSC Adv.*, 2023, **13**, 15640

Flower ball cathode assembled from Cu doped Co_3S_4/Ni_3S_2 ultrathin nanosheets in a photocatalytic fuel cell for efficient photoelectrochemical rifampicin purification and simultaneous electricity generation based on a CuO QDs/TiO_2/WO_3 photoanode†

Yuling Wang,[ab] Xiaolong Li,[ab] Yankun Fan,[ab] Jun Wu,[ab] Xin Wu,[ab] Ligang Xia, *[abc] Weifeng Yao,[abc] Qiang Wu,[abc] Yulin Min[abc] and Qunjie Xu*[abc]

Received 15th April 2023
Accepted 15th May 2023

DOI: 10.1039/d3ra02502k

rsc.li/rsc-advances

Herein, an efficient CuO QDs/TiO_2/WO_3 photoanode and a Cu doped Co_3S_4/Ni_3S_2 cathode were successfully synthesized. The optimized CuO QDs/TiO_2/WO_3 photoanode achieved a photocurrent density of 1.93 mA cm^{-2} at 1.23 *vs.* RHE, which was 2.27 times that of a WO_3 photoanode. The CuO QDs/TiO_2/WO_3-buried junction silicon (BJS) photoanode was coupled with the Cu doped Co_3S_4/Ni_3S_2 cathode to construct a novel photocatalytic fuel cell (PFC) system. The as-established PFC system showed a high rifampicin (RFP) removal ratio of 93.4% after 90 min and maximum power output of 0.50 mW cm^{-2}. Quenching tests and EPR spectra demonstrated that $^{\bullet}OH$, $^{\bullet}O_2^-$ and $^1O_2$ were the main reactive oxygen species in the system. This work provides a possibility to construct a more efficient PFC system for environmental protection and energy recovery in the future.

1. Introduction

Water is an indispensable and irreplaceable resource for social and economic development. While a large number of water resources are seriously polluted by organic pollutants, the purification of sewage has become an urgent problem.[1,2] Relevant studies have found that organic wastewater contains a large number of excellent electron donors,[3] which are ideal available energy sources.[4] Photocatalytic fuel cell (PFC) technology, as an extension of photocatalytic technology, has attracted extensive attention of researchers because it can recover the chemical energy in the process of wastewater treatment.[5,6] In a typical PFC system, the semiconductor photoanode generates electron–hole pairs under illumination, the organics are oxidized by holes on the surface of the anode and the electrons are transferred from the external circuit to the cathode to participate in reduction reaction.[7,8] Therefore, an excellent photoanode and cathode material can greatly improve the performance of a PFC system.

A photoanode with excellent photoelectrochemical (PEC) performance should meet the requirements of small band gap, appropriate energy band position, fast carrier separation and transport, high stability, *etc.* TiO_2 is the most popular n-type semiconductor with low cost, nontoxicity and high chemical stability. However, it only responds to ultraviolet light. While WO_3 can make up for this defect because of its good visible light response. Therefore, WO_3 and TiO_2 can form a heterostructure to improve the utilization of sunlight, and reduce the recombination of electrons and holes. In addition, quantum dots (QDs) with a particle size of several nanometers have strong light trapping ability and effectively promote charge transfer. In particular, CuO quantum dots have narrow band gap and wide optical response range.[9] Loading CuO quantum dots on the semiconductor surface can further reduce the recombination of photo-generated carriers, making the PEC performance of the photoanode increase greatly.

Nowadays, the research on cathode materials has become a scientific hotspot in this field. Zhang *et al.* synthesized a FeNi–OH/NF cathode to degradation phenol through $^{\bullet}OH$ obtained by reacting H_2O_2 with Fe^{2+}.[10] Qin *et al.* prepared a Co/CF cathode, which exhibited an excellent activity for PMS activation. And the $^{\bullet}OH$ and $SO_4^{\bullet-}$ were the main reactive species for acid orange 7 degradation.[11] Su *et al.* synthesized a Fe/$NiCo_2S_4$ cathode for

[a]*Shanghai Key Laboratory of Materials Protection and Advanced Materials in Electric Power, Shanghai Engineering Research Center of Energy-Saving in Heat Exchange Systems, Shanghai University of Electric Power, Shanghai 200090, China. E-mail: xialg82@shiep.edu.cn; xuqunjie@shiep.edu.cn*

[b]*College of Environmental and Chemical Engineering, Shanghai University of Electric Power, No. 2588 Changyang Road, Shanghai 200090, China*

[c]*Shanghai Institute of Pollution Control and Ecological Security, Shanghai, China*

† Electronic supplementary information (ESI) available. See DOI: https://doi.org/10.1039/d3ra02502k

tetracycline degradation. The doped Fe can react with H_2O_2 to produce more $^{\bullet}OH$ and $^{\bullet}O_2^-$ and maintain the stability of cathode.[12] We found that transition metal complexes, especially sulfides, have been widely studied and gained a lot of attention for oxygen reduction reaction. As a transition metal sulfide (TMS), Ni_3S_2 is widely used in energy storage applications, hydrogen evolution and supercapacitors as its electrical conductivity and high active specific surface area.[13–16] However, compared with the bimetallic sulfide heterostructure, the catalytic activity of Ni_3S_2 (a single metal sulfide) is still low. As is known to all, the catalytic activity of the electrode is not only related to the catalytic performance of the catalyst, but also depends on the surface properties like the wettability of catalyst surface and gas diffusion ability.[17] While the bimetallic sulfide heterostructure has the ability to improve hydrophilicity,[18] adjust the electronic transmission, and expose more active sites on the surface of catalytic materials.[19] Therefore, Co based sulfide (a second single metal sulfide) is chosen to further improve the catalytic activity of Ni_3S_2 because Co based sulfide possesses excellent oxygen species adsorption capacity and high oxidation capacity to generate reactive oxygen species.[20] The cathode modified by Co and Ni disulfide heterostructure can combine the advantages of the two substances to function as an excellent cathode in PFC system to realize the efficient degradation of pollutants.

Based on the ideas above, a Cu-doped Co_3S_4/Ni_3S_2 heterojunction cathode is prepared to establish a novel PFC system combined with CuO QDs/TiO_2/WO_3-buried junction silicon (BJS) photoanode. The CuO QDs/TiO_2/WO_3 photoanode displays an excellent PEC performance. The Co_3S_4/Ni_3S_2 heterojunction can not only provide a favorable interface for adsorption and activation of oxygen, but also promote electron transfer to take part in the process of oxygen reduction.[21] Cu as a guest material can optimize the microstructure of the material and adjust the conductivity and stability of the raw material.[22] The doping of copper increases the generation of ROSs and takes part in the circulation of Co^{3+}/Co^{2+} and Ni^{3+}/Ni^{2+}, leading to the improvement of the organic pollutant degradation performance, stability and power generation performance of the established system. As a comparison, Co_3S_4/Ni_3S_2 and Ni_3S_2 cathodes are also prepared to explore the possible degradation mechanism. The influence of Cu doping on the degradation performance of the PFC system are also studied. This study provides a possibility to construct a more efficient PFC system with excellent ability of wastewater degradation and electricity generation in the future.

2. Experimental section

2.1 Preparation of electrodes

Preparation processes of electrodes are shown in ESI.†

2.2 Characterization

A field emission scanning electron microscope (SEM, ZEISS Gemini 300) and a transmission electron microscope (TEM, TF20) were put to use to study the electrodes' morphology. X-ray diffraction (XRD, Bruker D8 Advance) was used to study the crystallographic structures of the electrodes. The X-ray photoelectron spectroscopy (XPS) spectra of the electrodes were obtained using an AXIS Ultra DLD (Kratos, Shimadzu, Japan) with Al Kα irradiation. The UV-vis diffuse reflectance spectra (UV-vis DRS) were determined by SHIMADZU UV2550 with $BaSO_4$ as the reference. The JC2000D3F goniometer was used to measure the contact angle. The N_2 adsorption–desorption method on the ASAP 2460 instrument (Micromeritics, USA) was used to gain the samples' Brunauer–Emmett–Teller (BET) surface.

2.3 PFC system setup and analytical method

The PEC performance of the photoanodes was tested using a CHI 660c electrochemical workstation with the prepared photoanode (an area of 1 cm^2 was exposed to light for testing) (working electrode), Ag/AgCl electrode (reference electrode) and Pt electrode (counter electrode). Experiments were conducted in a 0.1 M Na_2SO_4 solution (pH = 7) unless otherwise specified. A Xenon lamp with AM 1.5 filter glass was used as the light source (light intensity 100 mW cm^{-2}). Linear scanning voltammetry (LSV) plots were measured with a scan rate of 20 mV s^{-1} at bias voltages of −0.2 to 1.2 V *vs.* RHE. The electrochemical impedance spectroscopy (EIS) was measured in the frequency range of 0.01 to 10^5 Hz with an AC voltage (amplitude: 10 mV) of 0.6 V *vs.* RHE under the simulated solar light.

The degradation experiments were performed with a CuO QDs/TiO_2/WO_3-BJS photoanode and a prepared cathode without external bias under open circuit mode. Rifampicin (RFP) was used as a target pollutant. All degradation experiments were performed in 0.1 M Na_2SO_4 as the electrolyte (pH = 7). Before the reaction, the device performed a 30 min dark reaction and continuous aeration during the whole experiment. Using UV-vis Shimadzu UV-2600 spectrophotometer to determine the concentration of organic pollutants. The total organic carbon (TOC) was measured through a TOC sensor (Mettler Toledo 4000TOCe). In electrochemical (EC) degradation experiment, the working electrode was replaced by Pt electrode, and applying same |V bias| value in the Cu/Co_3S_4/Ni_3S_2 PFC system to it. The atomic absorption spectrophotometer (AAS, TAS-990, Persee) was used to determine the amount of dissolved metal ions. The whole PFC system were tested from −2.5 V to 0 V with the scan rate of 10 mV s^{-1} to obtain power output curves and power density curves (abscissas: $|V_{bias}|$, ordinates: $|J \times V_{bias}|$) of different cathodes. The CW-EPR spectrometer was used to obtain electron spin resonance spectra (ESR) to detect free radicals.

3. Results and discussion

3.1 Characterization of the photoanodes

Fig. 1 presents the morphologies of the prepared photoanodes. As can be seen from Fig. 1a, the WO_3 film is in rod shape and layered structure. The cross-sectional image demonstrates that WO_3 photoanode was vertically grown on the surface of FTO with a thickness of 1.0 μm. The top and cross-sectional SEM images of CuO QDs/TiO_2/WO_3 are demonstrated in Fig. 1 (b–d).

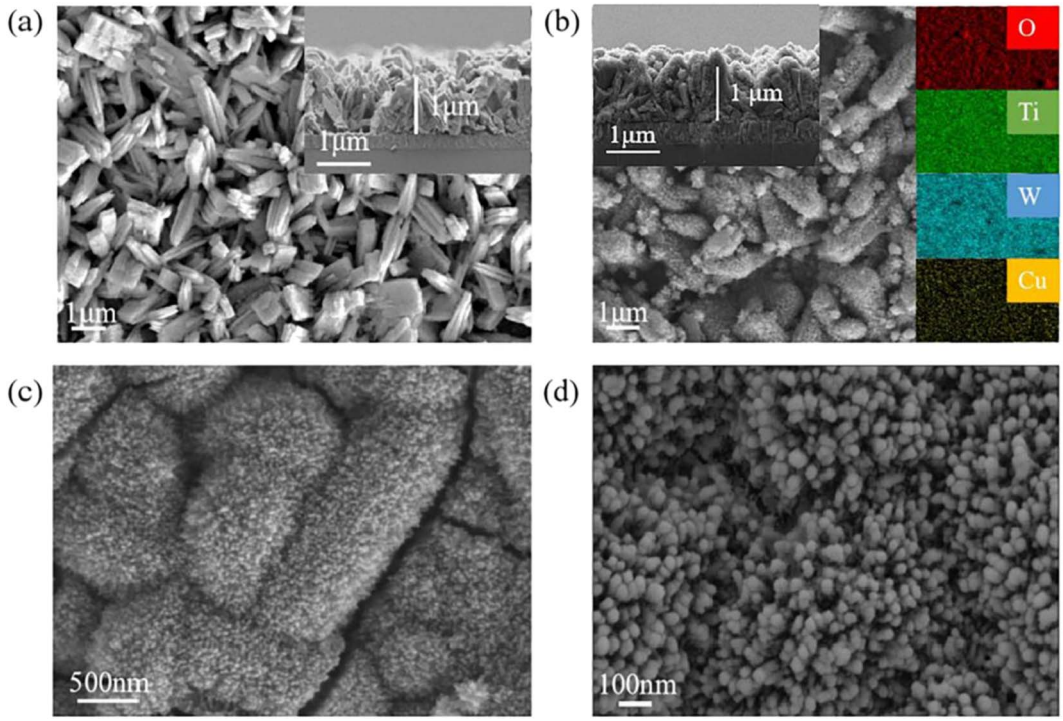

Fig. 1 (a) Top and cross-sectional SEM images of WO_3 photoanode. (b–d) Top and cross-sectional SEM images of CuO QDs/TiO_2/WO_3 at different magnifications.

From the EDS spectra of O, Ti, W and Cu in Fig. 1b (right), it can be seen that each element is evenly distributed on the surface of CuO QDs/TiO_2/WO_3 photoanode. In addition, the surface of WO_3 is covered by a layer of dense TiO_2 nanothorn with scattered CuO QDs outside. The lattice spacing of the CuO QDs/TiO_2/WO_3 photoanode was characterized by TEM (Fig. S1†). The lattice fringes of 0.38 nm and 0.37 nm are corresponding to the *d*-spacing value of the (002) plane and (020) plane of WO_3. The lattice fringe of 0.24 nm is corresponding to the (004) plane of TiO_2.[23] The lattice fringes of 0.34 nm and 0.36 nm are corresponding to the *d*-spacing value of the CuO.[24] The distribution of four elements in the EDS diagram proves the successful synthesis of the CuO QDs/TiO_2/WO_3 photoanode, and the CuO exists in the form of CuO quantum dots with a diameter less than 100 nm.

The XRD tests were used to further research the crystal structures of the prepared WO_3, WO_3/TiO_2, and CuO QDs/TiO_2/WO_3 photoanodes. As shown in Fig. 2a, the diffraction peaks which located at 30° are consistent with the SnO_2 contained in FTO. The diffraction peaks at 2θ of 23.6° and 24.4° are corresponding to the WO_3 (PDF #43-1035). The diffraction peak at 2θ of 32.1° can be attributed to TiO_2 (PDF #76-1934). The diffraction peaks in the range of 40° to 45° are consistent with monoclinic CuO (PDF #44-0706), and the relative intensity of the diffraction peaks is also minimal due to the small amount of CuO QDs modification. The XPS tests were performed to verify the valence of the elements on the surface of the CuO QDs/TiO_2/WO_3 photoanode (Fig. 2b). As shown in Fig. 2c–f, the peaks seated at the binding energies of 35.20 eV and 37.18 eV belong to W^{6+}, and the peaks seated at 458.74 eV and 464.36 eV belong to Ti^{4+}.[23] The peaks of Cu^{2+} located at 932.35 eV and 952.25 eV.[25] The peak of the binding energy of O element at about 530.50 eV belongs to each metal oxide containing WO_3, TiO_2 and CuO,[24] and the peaks at 532.06 eV and 533.44 eV are derived from SiO_2 in FTO and organic matter contaminated during sample preparation.

3.2 PEC performance of the photoanodes

In order to optimize the performance of the CuO QDs/TiO_2/WO_3 electrode, we compared the electrodes prepared with different concentrations of Cu^+ precursors (Fig. 3a). The photocurrent density of CuO QDs/TiO_2/WO_3 photoanode was measured by LSV. As we can see that the photocurrent density of prepared photoanode increased with the increase of Cu^+ concentration. It can reach 1.93 mA cm^{-2} at 0.6 V *vs.* Ag/AgCl (1.23 V *vs.* RHE) when the Cu^+ concentration was 0.05 M. But when the concentration continued to increase to 0.1 M, the photocurrent density started to decrease. Therefore, CuO QDs/TiO_2/WO_3 photoelectrode prepared by 0.05 M precursor is used for subsequent experiments. Fig. 3b shows the *J*–*v* curves of various photoanodes. Affected by the intrinsic structural defects of WO_3, a characteristic current is generated. The photocurrent density of WO_3 is 0.85 mA cm^{-2} at 1.23 V *vs.* RHE. After forming a heterojunction with TiO_2, the current density reaches 1.42 mA cm^{-2} at 1.23 V *vs.* RHE. However, the CuO QDs/TiO_2/WO_3 photoelectrode exhibits an excellent enhanced photocurrent (1.93 mA cm^{-2} at 1.23 V *vs.* RHE), indicating the superiority of CuO QDs/TiO_2/WO_3 photoelectrode.

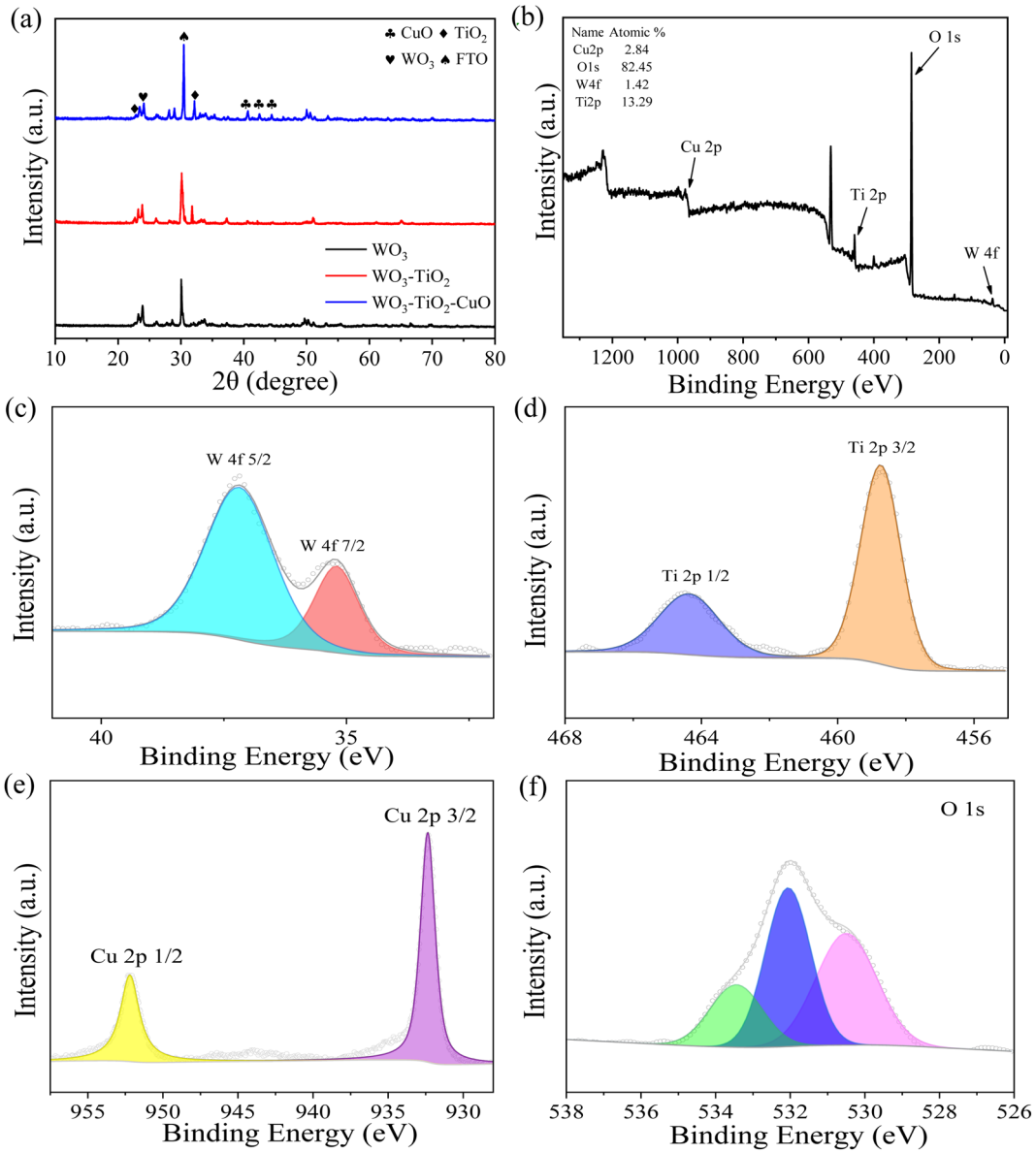

Fig. 2 (a) XRD patterns of various photoanodes. (b) Total XPS spectrum of CuO QDs/TiO_2/WO_3 photoanode. (c–f) XPS spectra of W, Ti, Cu and O in CuO QDs/TiO_2/WO_3 photoanode.

The light absorption abilities of WO_3, WO_3/TiO_2 and CuO QDs/TiO_2/WO_3 photoanodes are demonstrated in Fig. 3c. Compared with WO_3, the absorption in ultraviolet light range of WO_3/TiO_2 photoanode is significantly increased, which may be due to the nano level light trap composed of TiO_2 nano morphology covered on the surface of WO_3. After CuO QDs was decorated, a red shift is clearly observed in the absorption edge of CuO QDs/TiO_2/WO_3 photoanode. Meanwhile, the light harvesting of the CuO QDs/TiO_2/WO_3 photoanode displays a broad absorption. Moverover, WO_3, WO_3/TiO_2 and CuO QDs/TiO_2/WO_3 photoanodes have the band gaps of 2.70 eV, 2.68 eV and 2.59 eV (Fig. 3d), respectively.

The impedance tests were carried out in 0.1 M Na_2SO_4 solution (Fig. 3e). Compared with WO_3 photoanode, the impedance of WO_3/TiO_2 photoanode is significantly decreased. After the modification of CuO QDs, the whole photoanode showed the lowest impedance. These results indicate that CuO QDs/TiO_2 modification can effectively reduce the recombination of electron–hole and promote electron transfer. The *J*–*t* curve presents in Fig. 3f indicates the stability of CuO QDs/TiO_2/WO_3-BJS photoanode with a photocurrent density of 2.09 mA cm^{-2} without any external bias in a long time.

3.3 Characterization of the cathodes

The morphologies of the cathodes are shown in Fig. 4(a–c), S2 and S3.† Through vulcanization, the smooth surface of foam nickel becomes rough (Fig. S2†). When Co_3S_4 is introduced, clusters composed of dense nanosheets with holes grow on the surface of foam nickel (Fig. S3†). Since the ionic radius of Cu

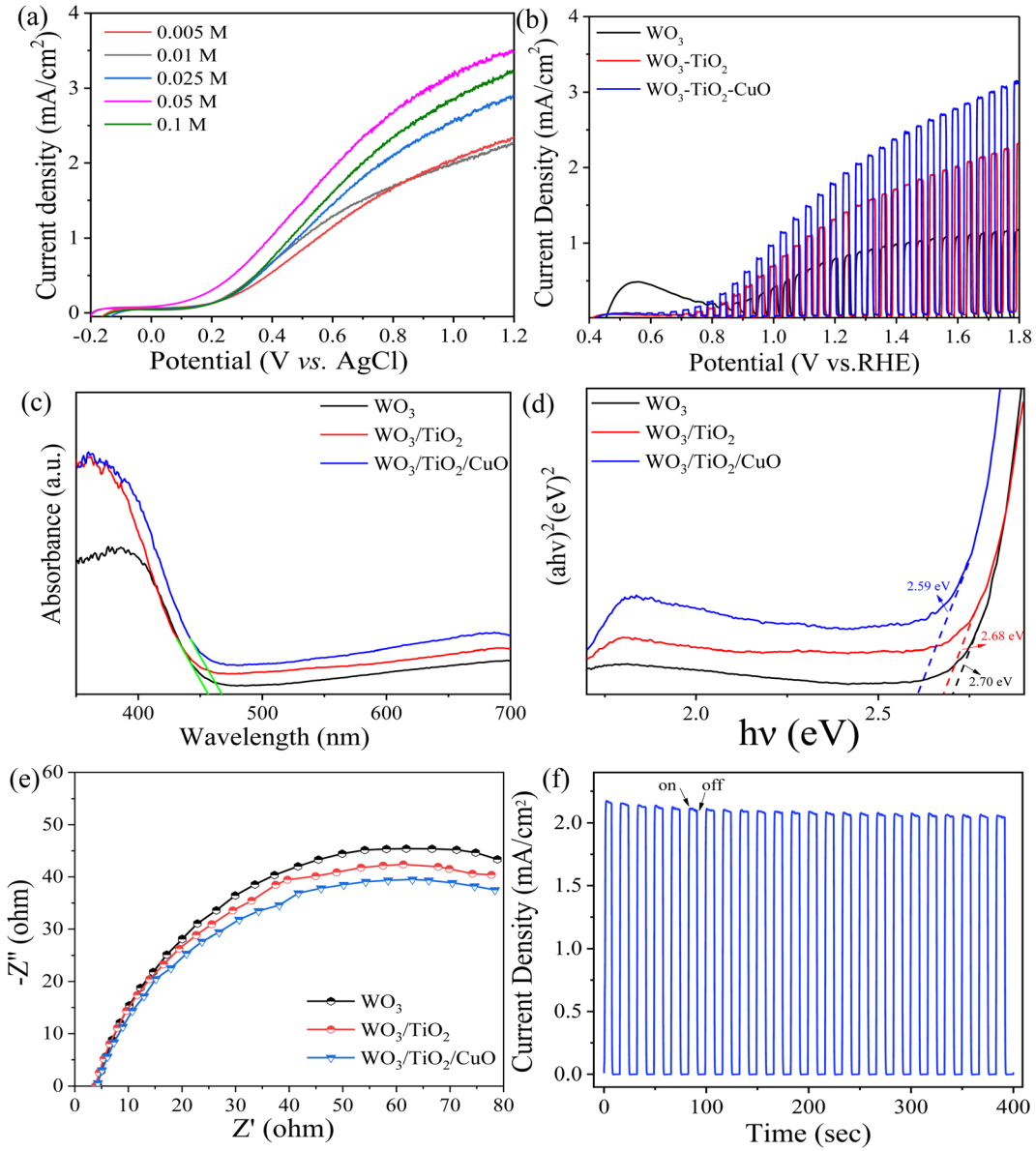

Fig. 3 (a) Linear voltammetric curves (LSV) of CuO QDs/TiO_2/WO_3 photoanodes prepared with different concentrations of Cu^+ precursors. (b) Chopped photocurrent-potential (*J*–*v*) curves of different photoanodes. (c) UV-vis absorption curves of various photoanodes and (d) the corresponding tauc plots of each photoanode. (e) Electrochemical impedance curves of each photoanode. (f) Photocurrent–time (*J*–*t*) plot of the CuO QDs/TiO_2/WO_3-BJS photoanode.

and Co ions are similar, Cu cations can be doped into Co_3S_4. The morphology of the Co_3S_4/Ni_3S_2 cathode changed into agglomerated flower balls with ultrathin petals after doped by Cu cation. This morphology will shorten the electron transfer distance to accelerate the electron transmission and improve the specific surface area to expose more active sites.[26] The EDS mapping images exhibit the uniform distribution of Co, Ni, Cu and S elements in $Cu/Co_3S_4/Ni_3S_2$ cathode (Fig. 4c insert). Fig. 4d shows the TEM image of $Cu/Co_3S_4/Ni_3S_2$, which indicates the synthesized $Cu/Co_3S_4/Ni_3S_2$ possessed an ultrathin structure. The lattice fringes of 0.27 nm and 0.23 nm are corresponding to the *d*-spacing value of the (222) plane of Co_3S_4 and (021) plane of Ni_3S_2 (Fig. 4e). The crystallographic structures of the cathodes are studied by XRD. As shown in Fig. 4f, the Ni foam has three distinct peaks which located at 44.3°, 51.7° and 76.2°. The diffraction peaks at 21.6°, 38.1°, 49.6°, 50.0°, and 68.8° are consistent with the (101), (021), (113), (211), and (303) crystal planes of Ni_3S_2 (PDF #44-1418). The other characteristic peaks at 32.8°, 38.2°, and 55.1° are assigned to the (222), (400), and (440) crystal planes of Co_3S_4 (PDF #73-1703). It is worth noting that a negative shift in peak positions is observed for $Cu/Co_3S_4/Ni_3S_2$, but no obvious diffraction peaks of Cu, which further proved that Cu ions are successfully doped into the lattice.[27–29] The corresponding cell parameters are shown in Table S1.† Moreover, the diffraction peak intensity of the doped samples become stronger as the Cu can change the

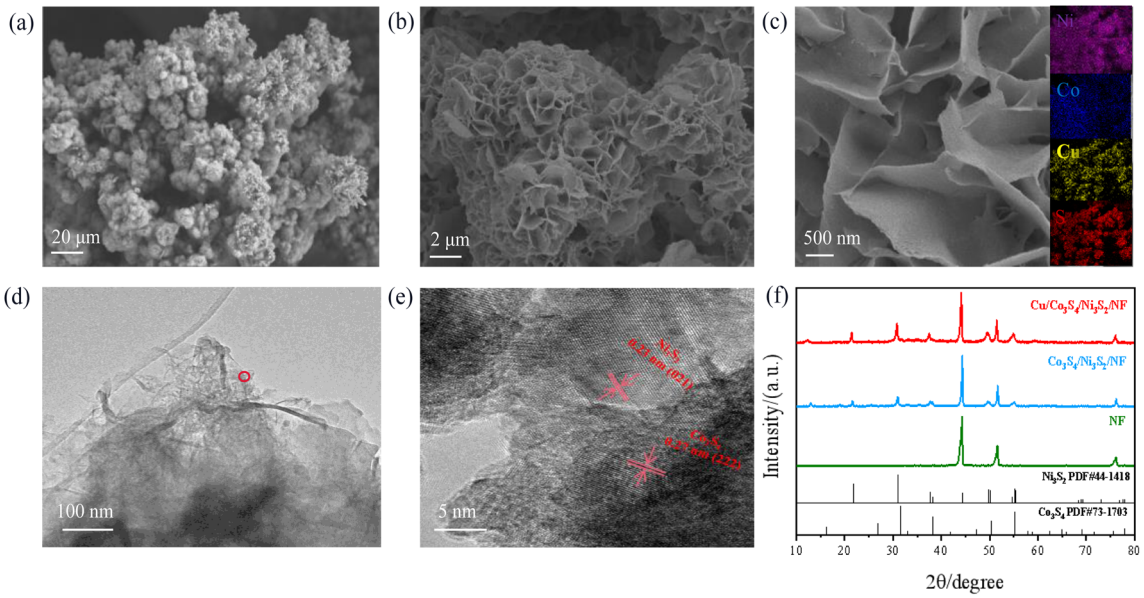

Fig. 4 (a–c) SEM images of Cu/Co_3S_4/Ni_3S_2 cathode (insert: EDS mapping images of Ni, Co, Cu and S). (d and e) TEM images of Cu/Co_3S_4/Ni_3S_2 (f) XRD patterns of prepared cathodes.

morphology of samples to promote nucleation, making the samples have high crystallinity.[30] The contact angle of the electrode is measured to evaluate the wettability of the surface. In Fig. S4,† the contact angle on pristine Ni foam is 123.33°, indicating that the hydrophilicity of Ni foam surface is poor (Fig. S4a†). After Ni_3S_2 formed on the surface, the hydrophilicity is improved with the contact angle decreases to 83.34° (Fig. S4b†). And the electrodes become completely hydrophilic after introduced Co_3S_4 and Cu/Co_3S_4 to Ni_3S_2 (Fig. S4c and d†).[31] The hydrophilic surface is conducive to the rapid penetration of electrolyte into the electrode surface while accelerate the diffusion of reactive oxygen species. In addition, we also conducted LSV measurements on the Cu/Co_3S_4/Ni_3S_2 cathode. As shown in Fig. S5a,† it can be seen that the two curves almost overlap, which is similar to the result shown in the reported work.[32] The chopping photocurrent curve of the Cu/Co_3S_4/Ni_3S_2 cathode was also tested (Fig. S5b†). It can be found that the Cu/Co_3S_4/Ni_3S_2 cathode almost has no photo-response.

3.4 Organic degradation properties in the established PFC systems

In order to evaluate the pollutant degradation ability of the established PFC systems, rifampicin is chosen as the target pollutant. The self-photodegradation of rifampicin is in Fig. S6.† As anions may interfere the catalytic degradation process by forming new oxidation species, the effects of different concentration of SO_4^{2-} were studied. It is clear that SO_4^{2-} showed negligible influence on the degradation of pollutant (Fig. S7a†). The effects of different concentrations of Na_2SO_4 on the power density of the system is also studied (Fig. S7b†). With the concentrations of Na_2SO_4 increasing from 0.05 M to 0.1 M, the P_{max} increases. When the concentration is higher than 0.1 M, P_{max} begins to decrease. This is because the separation efficiency of photogenerated charges of photoanode replaces the charge transfer efficiency in the solution as a key factor.[33] Therefore, 0.1 M Na_2SO_4 was selected as the supporting electrolyte in the experiment. Fig. 5a shows the degradation performance of systems with different cathodes. The degradation efficiencies of Ni foam, Ni_3S_2, Co_3S_4/Ni_3S_2 and Cu/Co_3S_4/Ni_3S_2 PFC systems are 42.2%, 54.3%, 75.2% and 93.4%. The TOC removal efficiency in Cu/Co_3S_4/Ni_3S_2 PFC system is about 70.1% after 90 min. The corresponding kinetic curves of different systems are shown in Fig. 5b, and the Cu/Co_3S_4/Ni_3S_2 PFC system has a maximum rate constant of 0.028 min^{-1}. It can be concluded that the Cu/Co_3S_4/Ni_3S_2 exhibits the most excellent catalytic performance. The BET specific surface areas of Co_3S_4/Ni_3S_2 and Cu/Co_3S_4/Ni_3S_2 cathodes are 5.90 $m^2\ g^{-1}$ and 9.53 $m^2\ g^{-1}$, which will endow Cu/Co_3S_4/Ni_3S_2 with higher catalytic activity by providing more active sites on catalyst.

To clarify the degradation effect of Cu/Co_3S_4/Ni_3S_2 cathode, the removal efficiency comparison between EC and PEC system is shown in Fig. S8.† The removal ratios in Cu/Co_3S_4/Ni_3S_2 EC and PEC systems are 47.2% and 93.4%, indicating that the Cu/Co_3S_4/Ni_3S_2 cathode has a significant function in degradation process. Furthermore, the Cu/Co_3S_4/Ni_3S_2 cathode also has a good stability as the degradation rate is still above 90% after five cycles (Fig. S9†).

3.5 Radical identification and possible catalytic mechanism in the PFC systems

3.5.1 Radical analysis in the PFC systems. Identifying the types of ROSs in the system is vital to reveal the degradation mechanism. As shown in Fig. 6a, *tert*-butanol (TBA), *p*-benzoquinone (*p*-BQ), furfuryl alcohol (FFA), EDTA-2Na and MeOH were used to quench $^{\cdot}OH$, $^{\cdot}O_2^-$, $^1O_2$, h^+ and $SO_4^{\cdot-}$. The removal efficiency is reduced to 71.3%, 47.5%, 57.1%, 82.9% and 72.1%

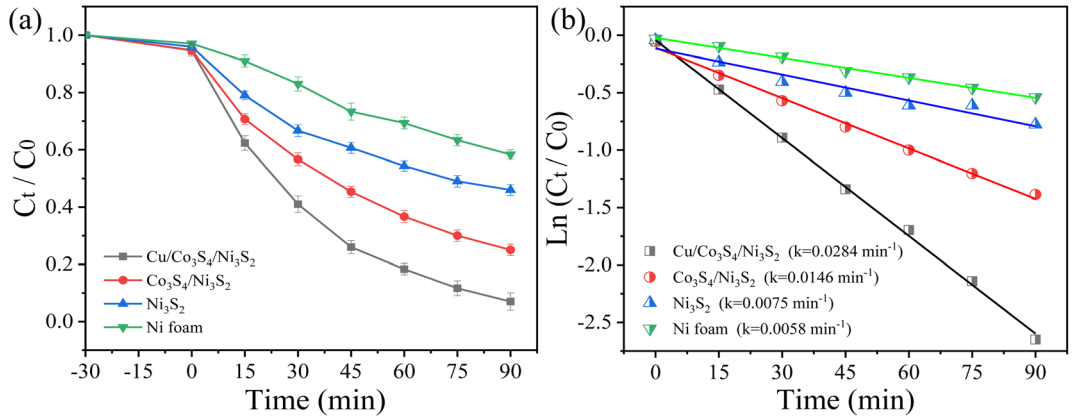

Fig. 5 (a) Degradation of 20 mg L^{-1} RFP in systems with different cathodes and (b) the corresponding kinetic curves.

in the presence of 20 mM of TBA, *p*-BQ, FA, EDTA-2Na and MeOH within 90 min, which mean that $^{\bullet}OH$, $^{\bullet}O_2^-$, $^1O_2$ and h^+ coexisted in the system. The quenching effect of MeOH is similar to that of TBA. Since MeOH can simultaneously quench $^{\bullet}OH$ and $SO_4^{\bullet-}$, it can be inferred that there is no $SO_4^{\bullet-}$ in the system. By comparing the degradation performance under different aeration conditions, it is found that the degradation efficiency of the electrode in N_2 environment is 30.4%, while the degradation efficiency is 48.7% without aeration because of the dissolved oxygen in water (Fig. 6b). Therefore, O_2 plays an important role to be reduced to $^{\bullet}O_2^-$ (eqn (1)) and H_2O_2 (eqn (2)) in the degradation process.

Due to $^{\bullet}OH$ can be obtained by reacting H_2O_2 with Cu^+ ions and Co^{2+} (eqn (3) and (4)), the concentration of H_2O_2 in the systems was determined (Fig. S10†). In Co_3S_4/Ni_3S_2 system, since the decomposition rate of H_2O_2 by Co^{2+} is greater than its production rate, the concentration of H_2O_2 decreases with time.[34] After doping of Cu ions, the concentration of H_2O_2 remains unchanged, which inferred that the decomposition rate of H_2O_2 by Cu and Co ions is equal to its production rate. The increase in H_2O_2 production rate is attributed to the Cu^+ which is beneficial for the delivery of electrons to oxygen molecules. When Cu^+ site absorbs oxygen molecules, the electron rich environment is conducive to the generation of H_2O_2 by

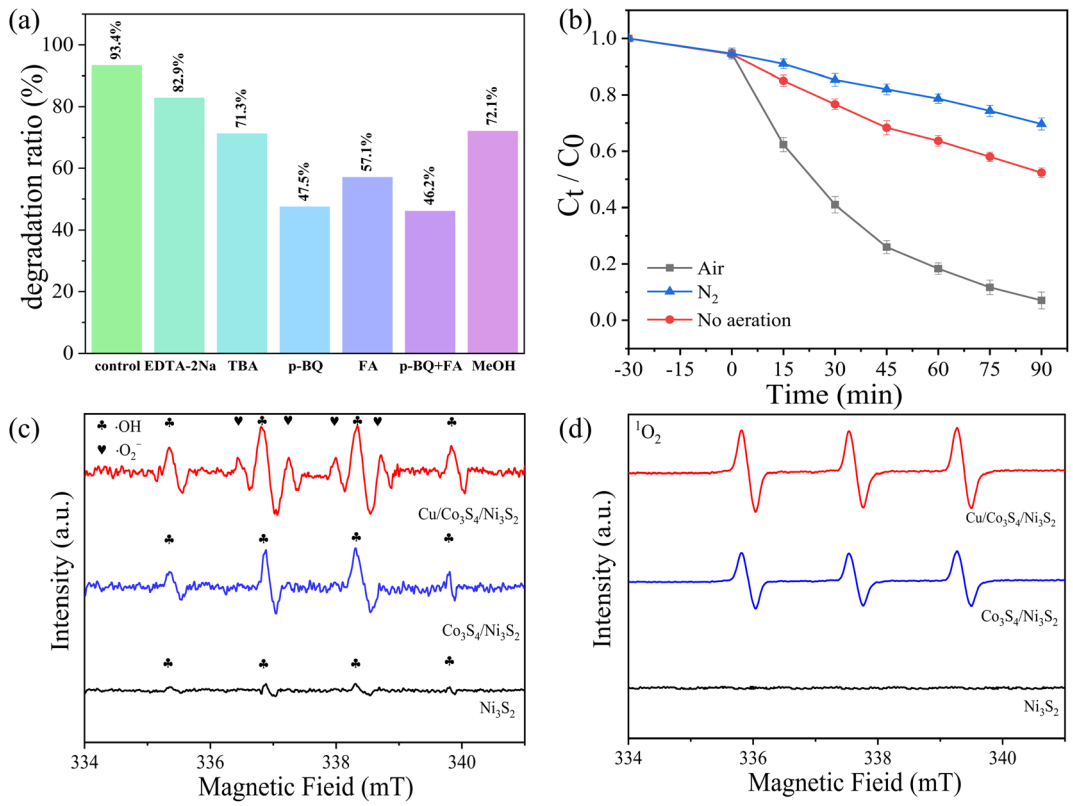

Fig. 6 (a) Effects of different ROSs scavengers on 20 mg L^{-1} RFP degradation in $Cu/Co_3S_4/Ni_3S_2$ PFC system. (b) Effect of electrode degradation under different aeration conditions. ROSs signals captured by (c) DMPO-$^{\bullet}OH$, $^{\bullet}O_2^-$ and (d) TEMP-$^1O_2$ in different systems.

H^+ attack.[35] To verify the source of $^1O_2$, *p*-BQ and FFA were added simultaneously (Fig. 6a). It was found that the inhibition effect when *p*-BQ and FFA coexisted is similar to that when *p*-BQ existed alone. Therefore, we speculate that the main source of $^1O_2$ was $^{\cdot}O_2^-$, and $^{\cdot}O_2^-$ can react with strongly oxidizing Co^{3+} to form $^1O_2$ (eqn (5)).[36,37]

To further explore the existence of $^{\cdot}OH$, $^{\cdot}O_2^-$, $^1O_2$, EPR tests were performed by DMPO and TEMP (Fig. 6c and d). In the Cu/Co_3S_4/Ni_3S_2 system, there are strong $^{\cdot}OH$, $^{\cdot}O_2^-$ and $^1O_2$ signals, and the source of $^{\cdot}O_2^-$ can also be obtained from eqn (6). However, in the Co_3S_4/Ni_3S_2 system, the signals of $^1O_2$ and $^{\cdot}OH$ become low. And there are no $^{\cdot}O_2^-$ signal in the Co_3S_4/Ni_3S_2 and Ni_3S_2 systems, because the $^{\cdot}O_2^-$ signal usually needs to be accompanied by a strong $^{\cdot}OH$ signal.[38,39] The weak $^{\cdot}OH$ signal of Ni_3S_2 system mainly comes from the oxidation of water by holes and there is no $^1O_2$ signals. According to the above conclusions, Cu doping can make the system generate more free radicals and the existence of Co^{3+} can promote the formation of $^1O_2$.

$$O_2 + e^- \rightarrow {}^{\cdot}O_2^- \quad (1)$$

$$O_2 + 2e^- + 2H^+ \rightarrow H_2O_2 \quad (2)$$

$$Cu^+ + H_2O_2 \rightarrow Cu^{2+} + {}^{\cdot}OH + OH^- \quad (3)$$

$$Co^{2+} + H_2O_2 \rightarrow Co^{3+} + {}^{\cdot}OH + OH^- \quad (4)$$

$$Co^{3+} + {}^{\cdot}O_2^- \rightarrow Co^{2+} + {}^1O_2 \quad (5)$$

$$Cu^{2+} + H_2O_2 \rightarrow Cu^+ + HO_2^{\cdot} + H^+ \quad (6)$$

3.5.2 XPS analysis. XPS analysis is carried out to study the degradation mechanism of Cu/Co_3S_4/Ni_3S_2 cathode. Fig. 7a shows the full spectrum of the electrode. In Fig. 7b, two major peaks centered at 780.18 eV and 796.08 eV can be assigned to Co^{3+}, and the peaks of Co^{2+} appeared at 782.08 eV and 797.68 eV.[38] The relative content of the Co^{3+} increases from 54.96% to 68.09%, and the Co^{2+} decreases from 45.04% to 31.91% after used. The Ni 2p peaks are divided into six peaks, the peaks located at 854.88 eV and 872.38 eV are attributed to Ni^{2+}, while the peaks at 856.08 eV and 874.08 eV are attributed to Ni^{3+}.[40,41] The relative content of Ni^{2+} increases from 58.02% to 63.84%, and the Ni^{3+} reduces from 41.98% to 36.16% (Fig. 7c). The two peaks centered at 931.97 eV and 951.71 eV can be assigned to Cu^+, the two weak peaks which located at 932.73 eV and 952.81 eV are correspond to Cu^{2+}. The initial relative content of Cu^+ is 33.29% and then becomes 42.45% after reaction, while the Cu^{2+} decreases from 66.71% to 57.55% (Fig. 7d).[42] The change of the content among these metal ions can be attributed to the participation of Cu^+/Cu^{2+} and Co^{2+}/Co^{3+} in the free radical chain reaction and the redox cycle between Cu^+/Cu^{2+}, $Ni^{2+}/Ni^{3+}$and Co^{2+}/Co^{3+} (eqn (7)–(9)). As displayed in Fig. 7e, the S 2p peaks at 161.08 eV and 162.28 eV are belong to M–S bonding, and the single peak at 168.08 eV is S–O bonding.[43] The content of M–S bond changes from 23.33% to 20.14%, indicating that a small portion of metal ions are dissolved during the reaction. Through the atomic absorption test, the concentration of Ni ions, Cu ions and Co ions are 0.21 ppm, 0.03 ppm and 0.4 ppm respectively, which are far lower than the standard. In Fig. 7f, the peaks at 531.38 eV and 532.48 eV are ascribed to adsorbed oxygen or surface hydroxyl groups (denoted as O_a), and adsorbed molecular water (denoted as O_H).[44] Due to the part of the adsorbed oxygen and surface hydroxyl were consumed, the relative content of O_a decreases from 82.34% to 70.88%. And the increase of O_H is attributed to the organic intermediates and mineralized products produced in the reaction process.

$$Co^{2+} + Ni^{3+} \rightarrow Co^{3+} + Ni^{2+} \quad (7)$$

$$Co^{2+} + Cu^{2+} \rightarrow Co^{3+} + Cu^+ \quad (8)$$

$$Ni^{3+} + Cu^+ \rightarrow Ni^{2+} + Cu^{2+} \quad (9)$$

3.6 Optimization of copper content

Fig. S11† shows the degradation performance of Cu/Co_3S_4/Ni_3S_2 electrodes with different copper content. The degradation performance increased with the increase of Cu content. The Cu/Co_3S_4/Ni_3S_2 electrode with 0.5 mmol Cu content has the best degradation performance of 93.4%. But when the Cu content continued to increase to 0.7 mmol, the degradation performance started to decrease. We infer that excessive Cu will make the formed nanosheets thicker and thus prolong the electron transfer path, leading to the poor degradation performance (Fig. S12†).

3.7 Power generation performance of the established PFC systems

Fig. S13† shows the *J*–*t* curve of Cu/Co_3S_4/Ni_3S_2–CuO QDs/TiO_2/WO_3-BJS system in the degradation process. The current density remains stable during the entire operation. The *J*–*v* curves of different cathode systems and the relevant power output curves are shown in Fig. S14 and S15.† The short circuit current density (J_{sc}) and open-circuit voltage (V_{oc}) of Cu/Co_3S_4/Ni_3S_2 are1.07 mA cm^{-2} and 2.49 V. By comparing the V_{oc} of different cathodes, it can be found that the modification of foam nickel has slight effect on V_{oc}. In addition, the Cu/Co_3S_4/Ni_3S_2 system shows an excellent power output performance with a maximum power density of 0.50 mW cm^{-2}. Fig. S16† presents the current output of the Cu/Co_3S_4/Ni_3S_2 system in simulated wastewater and 0.1 M Na_2SO_4 solution. It can be concluded that the current of the system is enhanced by degrading pollutants, and the electrons generated by organic matter oxidation will partly transfer through the external circuit to the counter electrode. In addition, different pollutants are selected as target pollutants. As shown in Table 1, the degradation ratio of all pollutants is above 90%, and it shows excellent TOC removal ratio. The P_{max} is between 0.50 and 0.59 mW cm^{-2}. These results demonstrate the outstanding performance of the Cu/Co_3S_4/Ni_3S_2–CuO QDs/TiO_2/WO_3-BJS system. In addition, compared with other existing PFC systems, our work has made further improvements in electric production and pollutant degradation (Table S2†).

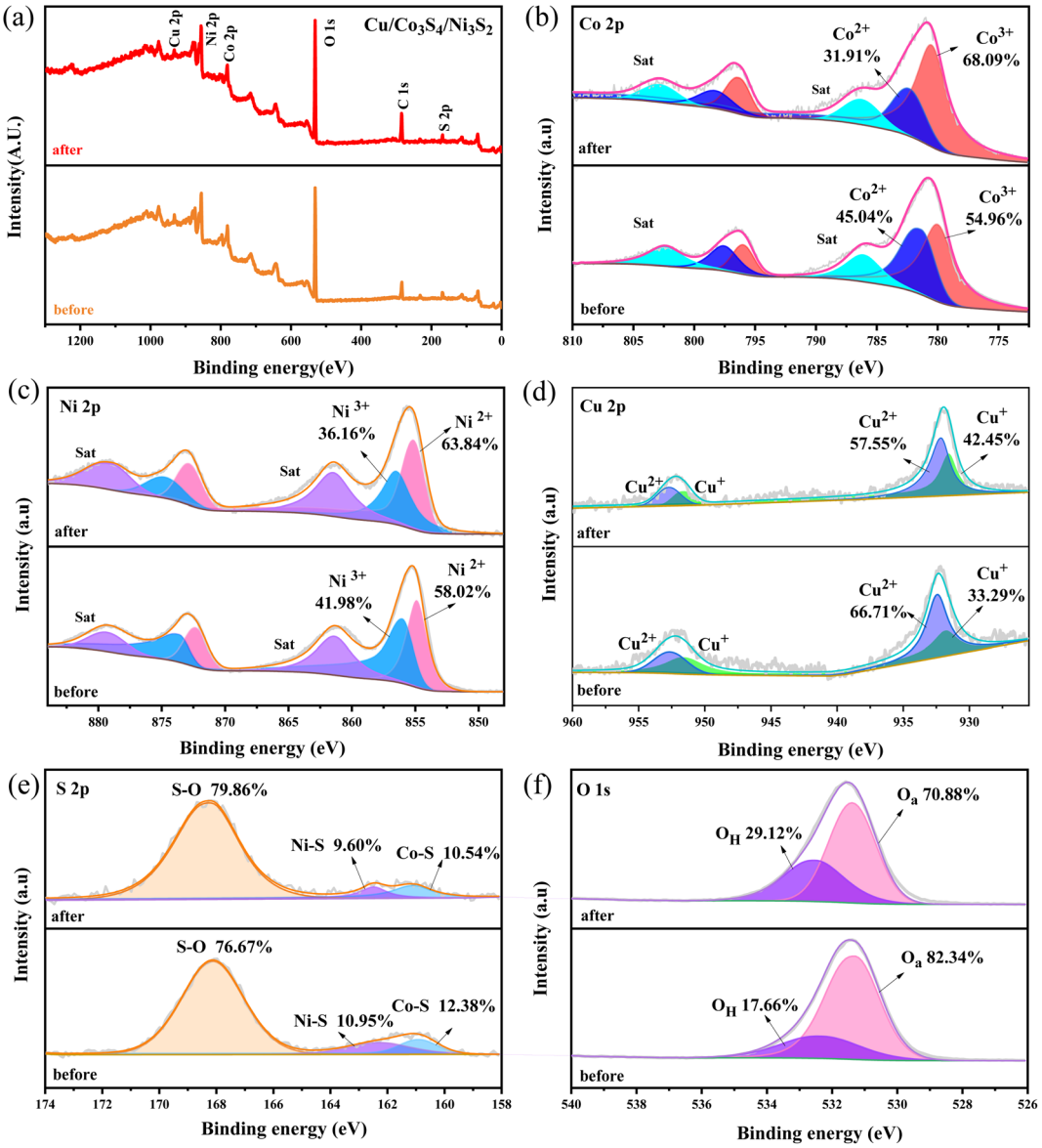

Fig. 7 XPS spectra of (a) $Cu/Co_3S_4/Ni_3S_2$, (b) Co 2p, (c) Ni 2p, (d) Cu 2p, (e) S 2p, (f) O 1s before and after reaction.

Furthermore, we analyzed the mechanism of power generation by organic oxidation. When light is irradiated, electrons and holes on the CuO QDs/TiO_2/WO_3 photoanode surface are separated (eqn (10)), leaving vacancies on the anode surface. Holes (h^+) oxidize H_2O to form $^{\bullet}OH$ (eqn (11)). h^+ and $^{\bullet}OH$ can oxidize organic pollutants (R–H) to generate organic free radical intermediates ($R^{\bullet}$) (eqn (12) and (13)). $R^{\bullet}$ itself is rich in electrons and possesses high energy and can release electrons to the cathode (eqn (14) and (15)). In addition, $R^{\bullet}$ can also generate low molecular weight organic matter (R') to improve the efficiency of electricity production by reacting with h^+ and $^{\bullet}OH$ (eqn (16) and (17)). Based on this, the oxidation of $R^{\bullet}$ and R' can jointly promote the power generation.

Table 1 Performance comparison of the $Cu/Co_3S_4/Ni_3S_2$–CuO QDs/TiO_2/WO_3-BJS PFC system in degrading various organic pollutants in 90 min

Pollutant (20 mg L^{-1})	V_{oc} (V)	J_{sc} (mA cm^{-2})	P_{max} (mW cm^{-2})	Degradation ratio (%)	TOC removal ratio (%)
RFP	2.49	1.07	0.50	93.4	70.1
TC	2.42	1.03	0.50	96.3	75.5
RhB	2.28	0.98	0.54	95.1	78.8
MB	2.35	0.95	0.59	94.4	77.6

$$\text{Photoanode} + h\nu \rightarrow h^+ + e^- \quad (10)$$

$$h^+ + H_2O \rightarrow {}^{\bullet}OH + H^+ \quad (11)$$

$$R\text{–}H + h^+ \rightarrow R^{\bullet} + H^+ \quad (12)$$

$$R\text{–}H + {}^{\bullet}OH \rightarrow R^{\bullet} + H_2O \quad (13)$$

$$R^{\bullet} \rightarrow R' + H^+ + e^- \quad (14)$$

$$R^{\bullet} \rightarrow R' + H_2O + e^- \quad (15)$$

$$R^{\bullet} + h^+ \rightarrow R' + H^+ \quad (16)$$

$$R^{\bullet} + {}^{\bullet}OH \rightarrow R' + H_2O \quad (17)$$

4. Conclusions

In this paper, a highly efficient CuO QDs modified TiO_2/WO_3 photoanode and a Cu doped Co_3S_4/Ni_3S_2 cathode were successfully synthesized. The optimized CuO QDs/TiO_2/WO_3 photoanode achieved a photocurrent density of 1.93 mA cm^{-2} at 1.23 *vs.* RHE, which was 2.27 times that of WO_3 photoanode. The CuO QDs/TiO_2/WO_3 photoanode was coupled with the Cu doped Co_3S_4/Ni_3S_2 cathode to construct a novel PFC system. The established PFC system showed a high RFP removal ratio of 93.4% after 90 min with a stable short-circuit current density of 1.07 mA cm^{-2}. The quenching tests and EPR spectra demonstrated that $^{\bullet}OH$, $^{\bullet}O_2^-$ and $^1O_2$ were the main ROSs in the system. The PFC system exhibits a stable degradation efficiency of several organic pollutants, which will expand its practical application in wastewater treatment and electrical energy generation.

Author contributions

Yuling Wang: writing – original draft, investigation, conceptualization, data curation, data analysis, validation. Xiaolong Li: investigation, validation. Yankun Fan: data curation, formal analysis. Jun Wu: validation, formal analysis. Xin Wu: data curation, formal analysis. Ligang Xia: validation, supervision, project administration, writing – review & editing, funding acquisition. Weifeng Yao: resources. Qiang Wu: resources. Yulin Min: resources. Qunjie Xu: resources, supervision, project administration, funding acquisition.

Conflicts of interest

The authors declare that they have no known competing financial interests or personal relationships that could have appeared to influence the work reported in this paper.

Acknowledgements

This work was supported by Science and Technology Commission of Shanghai Municipality (19DZ2271100) and Shanghai Institute of Pollution Control and Ecological Security.

References

1 B. Zhu, Q. Dong, J. Huang, D. Song, L. Chen, Q. Chen, C. Zhai, B. Wang, J. J. Klemes and H. Tao, *RSC Adv.*, 2023, **13**, 1594–1605.
2 Y. Wang, L. Qiu, S. Bao, F. Tian, J. Sheng, W. Yang and Y. Yu, *Sep. Purif. Technol.*, 2023, **316**, 123779.
3 M. Ghorbani, A. R. Nazar, M. Farhadian and S. Tangestaninejad, *Energy*, 2023, **272**, 127114.
4 W. Liu, S. Huo, X. Liu, Y. Wang, S. Xin, W. Fu, M. Gao and H. Xie, *Sep. Purif. Technol.*, 2023, **304**, 122336.
5 L. Dong, Y. Xu, D. Zhong, H. Chang, J. Li, Y. Liu and Z. Han, *Chemosphere*, 2023, **325**, 138399.
6 Q. Zeng, B. Gao, J. Tan, Q. Zhang, Y. Wen, Q. Zhang, Y. Cao, Z. Xiong, R. Oh and S. Zhao, *J. Environ. Chem. Eng.*, 2023, **11**, 109353.
7 S. M. Lam, J. C. Sin, H. Zeng, H. Lin, H. Li, Z. Qin, J. W. Lim and A. R. Mohamed, *Sep. Purif. Technol.*, 2021, **265**, 118495.
8 Y. Sun, L. Shen, Q. Qin, L. Jiang, Y. Su, Y. Wang, L. Xia, S. Lin, W. Yao, Q. Wu and Q. Xu, *Chemosphere*, 2022, **291**, 132911.
9 Y. Jiang, J. Guo, X. Li, G. Wu, M. Mu and X. Yin, *Sol. Energy*, 2022, **231**, 705–715.
10 F. Zhang, L. Zhou, S. Ma, P. Li, X. Zhang and L. Lei, *Sep. Purif. Technol.*, 2023, **314**, 123604.
11 Q. Qin, J. Zhang and Y. Dong, *Mater. Lett.*, 2023, **335**, 133833.
12 Y. Su, Y. Wang, L. Xia, W. Yao, Q. Wu, Y. Min and Q. Xu, *Chem. Eng. J.*, 2022, **449**, 137867.
13 N. Zhang, Y. Li, R. Zhang, S. Huang, F. Wang, M. Tang and J. Liu, *J. Colloid Interface Sci.*, 2023, **642**, 479–487.
14 Y. Deng, X. Tong, N. Pang, Y. Zhou, D. Wu, S. Xu, D. Xiong, L. Wang and P. K. Chu, *Appl. Surf. Sci.*, 2022, **572**, 151442.
15 M. Luo, S. Liu, W. Zhu, G. Ye, J. Wang and Z. He, *Chem. Eng. J.*, 2022, **428**, 131055.
16 W. Wei, B. Liu, Y. Gan, H. Ma, D. Chen, J. Qi and S. Li, *Surf. Coat. Technol.*, 2020, **403**, 126442.
17 Y. Yao, J. He, L. Ma, J. Wang, L. Peng, X. Zhu, K. Li and M. Qu, *J. Colloid Interface Sci.*, 2022, **616**, 287–297.
18 W. Chen, M. Zhang, Y. Liu, X.-M. Yao, P.-Y. Liu, Z. Liu, J. He and Y.-Q. Wang, *Appl. Catal., B*, 2022, **312**, 121432.
19 S. Kim, K. Min, H. Kim, R. Yoo, S. E. Shim, D. Lim and S.-H. Baeck, *Int. J. Hydrogen Energy*, 2022, **47**, 8165–8176.
20 J. Luo, Y. Zhou, Y. Tuo, Y. Gu, X. Wang, Q. Guo, C. Chen, D. Wang, S. Wang and J. Zhang, *Appl. Mater. Today*, 2022, **26**, 101311.
21 Q. Wu, A. Dong, C. Yang, L. Ye, L. Zhao and Q. Jiang, *Chem. Eng. J.*, 2021, **413**, 127482.
22 X. Xu and J. I. Han, *Surf. Interfaces*, 2022, **30**, 101896.
23 Q. Zeng, J. Bai, J. Li, B. Zhou and Y. Sun, *Nano Energy*, 2017, **41**, 225–232.
24 C. Wang, J. Tang, X. Zhang, L. Qian and H. Yang, *Prog. Nat. Sci.*, 2018, **28**, 200–204.
25 Z. Hussain, M. A. Salim, M. A. Khan and E. E. Khawaja, *J. Non-Cryst. Solids*, 1989, **110**, 44–52.
26 H. Su, S. Song, S. Li, Y. Gao, L. Ge, W. Song, T. Ma and J. Liu, *Appl. Catal., B*, 2021, **293**, 120225.

27 J. Wei, X. Feng, X. Hu, J. Yang, C. Yang and B. Liu, *Colloids Surf., A*, 2021, **631**, 127754.
28 P. Sahoo, A. Sharma, S. Padhan and R. Thangavel, *Superlattices Microstruct.*, 2021, **159**, 107050.
29 H. Esgin, Y. Caglar and M. Caglar, *J. Alloys Compd.*, 2022, **890**, 161848.
30 S. I. Abbas, S. F. Hathot, A. S. Abbas and A. A. Salim, *Opt. Mater.*, 2021, **117**, 111212.
31 Q. Kong, N. Fan, S. Chen, X. Wu, L. Liu, R. Lang, Z. Gao, H. Guan, C. Dong and G. Chen, *J. Electroanal. Chem.*, 2021, **895**, 115516.
32 Q. Sun, S. Wu, D. You, T. Zhang and L. Dong, *Appl. Surf. Sci.*, 2019, **467**, 825–835.
33 L. Li, J. Bai, S. Chen, Y. Zhang, J. Li, T. Zhou, J. Wang, X. Guan and B. Zhou, *Chem. Eng. J.*, 2020, **399**, 125839.
34 Y. Zou, H. Qi and Z. Sun, *Chemosphere*, 2022, **296**, 134072.
35 S. Hu, X. Qu, P. Li, F. Wang, Q. Li, L. Song, Y. Zhao and X. Kang, *Chem. Eng. J.*, 2018, **334**, 410–418.
36 J. Ji, Q. Yan, P. Yin, S. Mine, M. Matsuoka and M. Xing, *Angew. Chem., Int. Ed. Engl.*, 2020, **60**, 2903–2908.
37 Y. Yang, L. Xu and J. Wang, *Chem. Eng. J.*, 2021, **425**, 131497.
38 P. Hong, Z. Wu, D. Yang, K. Zhang, J. He, Y. Li, C. Xie, W. Yang, Y. Yang, L. Kong and J. Liu, *Chem. Eng. J.*, 2021, **421**, 129594.
39 L. Khachatryan, E. Vejerano, S. Lomnicki and B. Dellinger, *Environ. Sci. Technol.*, 2011, **45**, 8559–8566.
40 T. Wang, W. Ma, Y. Zhang, J. Guo, T. Li, S. Wang and D. A. Yang, *J. Energy Storage*, 2021, **35**, 102319.
41 X. Li, S. Zhao, G. Qu, X. Wang, P. Hou, G. Zhao and X. Xu, *J. Mater. Sci. Eng.*, 2022, **118**, 190–198.
42 J. Tang and J. Wang, *Chem. Eng. J.*, 2019, **375**, 122007.
43 X. Cui, Z. Xie and Y. Wang, *Nanoscale*, 2016, **8**, 11984–11992.
44 C. Chen, L. Liu, J. Guo, L. Zhou and Y. Lan, *Chem. Eng. J.*, 2019, **361**, 1304–1316.